

Slicer Networks

Hang Zhang¹, Renjiu Hu¹, Xiang Chen²,
Rongguang Wang³, Dongdong Liu⁴ and Gaolei Li⁵

¹Cornell University ²Hunan University ³University of Pennsylvania
⁴New York University ⁵Shanghai Jiao Tong University

Abstract

In medical imaging, scans often reveal objects with varied contrasts but consistent internal intensities or textures. This characteristic enables the use of low-frequency approximations for tasks such as segmentation and deformation field estimation. Yet, integrating this concept into neural network architectures for medical image analysis remains underexplored. In this paper, we propose the Slicer Network, a novel architecture designed to leverage these traits. Comprising an encoder utilizing models like vision transformers for feature extraction and a slicer employing a learnable bilateral grid, the Slicer Network strategically refines and upsamples feature maps via a splatting-blurring-slicing process. This introduces an edge-preserving low-frequency approximation for the network outcome, effectively enlarging the effective receptive field. The enhancement not only reduces computational complexity but also boosts overall performance. Experiments across different medical imaging applications, including unsupervised and keypoints-based image registration and lesion segmentation, have verified the Slicer Network’s improved accuracy and efficiency.

1 Introduction

Recent developments in medical image analysis have benefited from the integration of Convolutional Neural Networks (ConvNets) [He *et al.*, 2016] and vision-based transformers [Liu *et al.*, 2021; Dosovitskiy *et al.*, 2021]. These techniques have enhanced various tasks including lesion segmentation [Isensee *et al.*, 2021; Zhang *et al.*, 2023c], deformable image registration [Balakrishnan *et al.*, 2019; Zhang *et al.*, 2023a], and inverse reconstruction [Genzel *et al.*, 2022]. Two vital factors to their effectiveness are: 1) The access to large-scale datasets [Ridnik *et al.*, 2021; Sun *et al.*, 2017] which are crucial for pretraining these backbone networks, and 2) The increased *effective receptive field (ERF)* [Luo *et al.*, 2016] resulting from stacking deeper convolutional layers or using larger kernels [Ding *et al.*, 2022; Liu *et al.*, 2022] in ConvNets and the integration of self-attention mechanisms in transformers [Vaswani *et al.*, 2017; Liu *et al.*, 2021; Dosovitskiy *et al.*, 2021; Wang *et al.*, 2021].

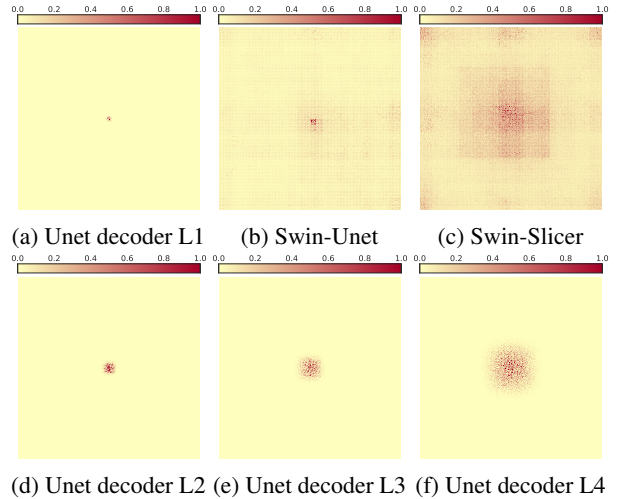


Figure 1: *Effective Receptive Field (ERF)* visualizations [Luo *et al.*, 2016] across architectures: U-Net (a, d, g, j), Swin-Unet (b), Swin-Slicer (c). Darker and more widely spread regions indicate larger ERFs. Swin-Unet and Swin-Slicer feature maps are presented pre-softmax, while Unet utilizes decoder feature maps, with L4 to L1 showing increased spatial sizes via upsampling. Our slicer network enhances the ERF compared to standard Unet layers.

Building upon these foundational backbones, a variety of U-shaped encoder-decoder networks [Ronneberger *et al.*, 2015] have been developed, as detailed in works like [Cao *et al.*, 2022; Chen *et al.*, 2021; Rahman and Marculescu, 2023; Tang *et al.*, 2022; Lee *et al.*, 2022]. These networks typically combine an encoder with cascaded decoders, connected via shortcuts. This design, while proficient in detailing fine attributes, tends to diminish the ERF, which may result in reduced contextual understanding (refer to Fig. 1). This study aims to tackle this limitation from a network architecture perspective, seeking to enhance both the effectiveness and efficiency of certain medical image analysis tasks.

Imaging modalities such as Magnetic Resonance Imaging (MRI), Computed Tomography (CT) and dermoscopy produce numerous images for inspection on specific targets like cardiac ventricles or skin lesions. These images usually require registration or segmentation before detailed analysis. Many exhibit consistent internal contrasts and textures within objects and clear variations across boundaries. This characteristic

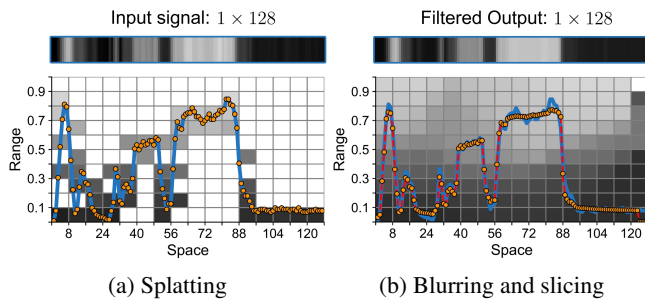


Figure 2: Visual illustration of the traditional tri-phase bilateral grid process comprising splatting, blurring, and slicing on a 1D signal. **Splatting:** Employs a nearest sampling kernel to transform image signals, normalized to (0,1) from a dimension of 1×128 into a 16×10 sparse spatial-range grid using sampling rates $s_s = 8$ and $s_r = 0.1$. **Blurring:** Applies Gaussian filters with $\sigma = 1$ to both spatial and range dimensions, corresponding to $\sigma_s = \sigma \times s_s$ and $\sigma_r = \sigma \times s_r$ in the initial image space. **Slicing:** Utilizes a bilinear sampling kernel, normalized via homogeneous coordinates. (a) Depicts the bilateral grid aligned with the input 1D signal, with orange dots showing projected intensities linked by a blue line. (b) Exhibits the Gaussian-blurred grid and filtered output 1D signal; orange dots are sliced intensities, contrasted against the original blue line using a dashed red line.

imparts a *piece-wise smooth* quality to both the images and their outputs, including segmentation masks and deformation fields. With careful preservation of object boundaries, accurate low-frequency approximations could be effective without losing critical details. For example, the bilateral grid [Paris and Durand, 2006; Chen *et al.*, 2007] and its subsequent variants [Adams *et al.*, 2009; Gastal and Oliveira, 2012; Gharbi *et al.*, 2017] have been widely used to accelerate megapixel image processing tasks via low-frequency approximations in high-dimensional grid space. Fig. 2 illustrates how image signals are projected in this context. Addressing the outlined challenges and characteristics leads to an assumption and two pivotal questions: **Assumption:** Medical imaging tasks with *piece-wise smooth* inputs and outputs lend themselves to effective low-frequency feature approximation. **Q1:** How can we enlarge the network’s ERF without losing critical details? **Q2:** Is it possible to reduce computational demands for resource-limited clinical settings?

To tackle the questions within the assumption, we introduce the Slicer Network, a novel architecture that enhances the ERF and boosts performance of medical application, providing an alternative alongside the traditional encoder-decoder networks. This framework is composed of two components: an encoder, adopted from established backbone architectures like Residual Network (ResNet) [He *et al.*, 2016] and Vision Transformers (ViTs) [Dosovitskiy *et al.*, 2021], and a slicer network with a learnable bilateral grid. The encoder creates feature maps that abstract and compress input images into low-resolution representations; the slicer then upsamples these feature maps, using a guidance map derived from raw images, to produce outputs that maintain object boundary integrity. The Slicer Network is similar to a combination of bilateral grid [Paris and Durand, 2006; Chen *et al.*, 2007] and joint bilateral upsampling [Kopf *et al.*,

2007], but it operates within a differentiable neural network context.

In our study, we evaluate our method across three medical imaging tasks: unsupervised cardiac MRI registration, keypoints-based lung CT registration, and dermoscopy-based skin lesion segmentation. Key findings include:

- The Slicer Network effectively expands the ERF while preserving boundary details, demonstrating superior performance in cardiac registration and skin lesion segmentation compared to other leading methods.
- The integration of a learnable bilateral grid enables zero-shot learning for keypoints-based lung CT registration, enhancing performance beyond conventional methods.
- In applications with *piece-wise smooth* inputs and outputs, like cardiac registration, our approach can significantly reduce computational demands by at least 80% while maintaining similar accuracy.

2 Related Work

2.1 Bilateral Grid and High-Dimensional Filtering

The original bilateral filter, as proposed by [Smith and Brady, 1997] and [Tomasi and Manduchi, 1998], enhances image quality by replacing each pixel with a weighted average of neighboring pixels. These weights are determined by both the spatial proximity within the image plane (*spatial domain S*) and the similarity in intensity values (*range domain R*). While this technique is effective at edge-preserving image manipulation, its native form suffers from slow processing speeds. To address this, advancements such as the bilateral grid [Paris and Durand, 2006; Chen *et al.*, 2007], Gaussian KD-Trees [Adams *et al.*, 2009] and adaptive manifolds [Gastal and Oliveira, 2012] have emerged. These techniques accelerate the bilateral filtering process by projecting original signals into a smaller yet higher-dimensional space, enabling real-time performance. Subsequently, such techniques have been adapted into neural networks for tasks like scene-dependent image transformation [Gharbi *et al.*, 2017] and stereo matching [Xu *et al.*, 2021]. However, their usage in tasks such as image segmentation and image registration in the medical domain is limited. Innovations like bilateral neural networks [Jampani *et al.*, 2016] and the fast bilateral solver [Barron and Poole, 2016] have sought to harness the potential of neural networks for these complex tasks, yet their applicability is still confined.

2.2 Learning with Differentiable Transformations

Grid Sampling (GS) [Jaderberg *et al.*, 2015] has empowered neural networks with transformation capabilities via differentiable interpolation. However, it is not suitable for transformations involving integration or summing, such as the Hough [Ballard, 1981; Lin *et al.*, 2020; Zhao *et al.*, 2021] and Radon [Helgason and Helgason, 1999] transforms and bilateral grid creation [Paris and Durand, 2006; Chen *et al.*, 2007]. [Zhang *et al.*, 2023b] introduces the Deep Directed Accumulator (DeDA) to address this limitation, establishing a complementary relationship with GS. GS “pulls” values to each cell in the target feature map from the source, whereas DeDA “pushes” values from each cell in the source to

the target feature map. Essentially, GS samples, while DeDA accumulates values from the source. When applied with proper geometric parametrization, the integration transformation highlights key geometric structures like lines [Lin *et al.*, 2020; Zhao *et al.*, 2021] and circles [Zhang *et al.*, 2023b] in new representations. Combined, DeDA and GS complete a forward-backward cycle in dense mapping tasks. Within our Slicer Network, DeDA constructs a differentiable bilateral grid, and GS performs slicing from this grid.

3 Method

In this section, we present the Slicer Network, starting with the traditional bilateral grid basics. We then explore the slicer network which integrates a differentiable cross-bilateral grid in neural networks using DeDA and GS. For simplicity and without loss of generality, we illustrate our framework using a 2-dimensional spatial domain.

3.1 Preliminaries

We start this section with a brief review of the process of implementing cross-bilateral filtering via a bilateral grid [Paris and Durand, 2006; Chen *et al.*, 2007] (ref to Fig. 2 for an example). Consider a guidance image $\mathbf{G}^r \in \mathbb{R}^{h \times w}$ normalized to the range $(0, 1)$, and an input image $\mathbf{I} \in \mathbb{R}^{h \times w}$. Let s_s and s_r denote the sampling rates in the spatial domain \mathcal{S} and the range domain \mathcal{R} , respectively. We can establish a bilateral grid $\Gamma \in \mathbb{R}^{\lfloor \frac{h}{s_s} \rfloor \times \lfloor \frac{w}{s_s} \rfloor \times \lfloor \frac{1}{s_r} \rfloor}$. This grid is initially set to zero and then updated by accumulating homogeneous coordinates:

$$\Gamma \left(\left[\frac{x}{s_s} \right], \left[\frac{y}{s_s} \right], \left[\frac{\mathbf{G}(x, y)}{s_r} \right] \right) += (\mathbf{I}(x, y), 1), \quad (1)$$

where x, y are coordinates, and $\lfloor \cdot \rfloor$ is the rounding operation.

The process described in Eq. (1) is known as splatting, wherein image signals are projected onto the higher-dimensional spatial-range domain $\mathcal{S} \times \mathcal{R}$. Any function f , including neural networks that inputs the constructed grid Γ , can be utilized to manipulate the grid, resulting in $\tilde{\Gamma} = f(\Gamma)$. For convolution operations, filtering within $\mathcal{S} \times \mathcal{R}$ respects locality both in the spatial and range domains. Subsequently, slicing is executed to formulate a new image by accessing the grid at locations $\left(\frac{x}{s_s}, \frac{y}{s_s}, \frac{\mathbf{G}(x, y)}{s_r} \right)$ through linear interpolation.

3.2 Differentiable Splatting and Slicing

Adopting notations from prior research [Jaderberg *et al.*, 2015; Zhang *et al.*, 2023b], we formulate the splatting and slicing operations as outlined below. When dealing with multi-channel inputs, the transformation process is independently applied to each channel. Our discussion primarily focuses on the spatial dimensions of these components for clarity. Although we demonstrate using 2D images and 3D grids, adapting this to 3D volumes and 4D grids is straightforward.

Splatting. Given a source feature map $\mathbf{U} \in \mathbb{R}^{H \times W}$ and a target $\Gamma \in \mathbb{R}^{H' \times W' \times R}$, with H, W as input and H', W' as output spatial dimensions, and R as the range dimension size. A sampling grid $\mathbf{G} \in \mathbb{R}^{H \times W \times 3} = (\mathbf{G}^x, \mathbf{G}^y, \mathbf{G}^r)$, with $\mathbf{G}^x, \mathbf{G}^y$ as mesh grids and \mathbf{G}^r as the guidance map, along

with a kernel function $\mathcal{K}(\cdot)$, are used. The value in the bilateral grid Γ at cell (i, j, k) is defined as:

$$\Gamma_{ijk} = \sum_{(n,m) \in \mathcal{S}} \mathbf{U}_{nm} \mathcal{K}(\mathbf{G}_{nm}^x, i) \mathcal{K}(\mathbf{G}_{nm}^y, j) \mathcal{K}(\mathbf{G}_{nm}^r, k), \quad (2)$$

where \mathcal{S} denotes the spatial domain, and the kernel function $\mathcal{K}(\cdot)$ can be any predefined kernel, like the linear sampling kernel $\mathcal{K}(p, q) = \max(0, 1 - |p - q|)$. Eq. (2) is a tensor mapping function by $\mathcal{D} : (\mathbf{U}, \mathbf{G}; \mathcal{K}) \mapsto \Gamma$. with a linear kernel, both \mathbf{G} and \mathbf{U} backpropagate gradients, unlike the nearest kernel where only \mathbf{U} does. Different from the original bilateral grid which uses nearest kernel for grid creation, we use a linear kernel and found it to be more effective.

Slicing. Slicing, the symmetric operation to splatting, is a crucial step that generates the piece-wise smooth output. For the 'blurred' bilateral grid $\tilde{\Gamma} \in \mathbb{R}^{H' \times W' \times R}$, we determine the value of a specific cell (n, m) in the sliced feature map $\mathbf{V} \in \mathbb{R}^{H \times W}$ as following:

$$\mathbf{V}_{nm} = \sum_{(i,j,k) \in \mathcal{S} \times \mathcal{R}} \tilde{\Gamma}_{ijk} \mathcal{K}(\mathbf{G}_{nm}^x, i) \mathcal{K}(\mathbf{G}_{nm}^y, j) \mathcal{K}(\mathbf{G}_{nm}^r, k), \quad (3)$$

Here, \mathcal{R} denotes the range domain, with other parameters as in Eq. (2). The main distinction between Eq. (2) (splatting) and Eq. (3) (slicing) is data flow direction. In splatting, each cell Γ_{ijk} aggregates values from the source feature map that correspond to its location. Conversely, in slicing, each cell \mathbf{V}_{nm} identifies its corresponding location in the source feature map and retrieves the value from there. This grid process enables edge-aware functionality. Gradient details for both equations are in [Jaderberg *et al.*, 2015; Zhang *et al.*, 2023b].

Homogeneous Coordinates. For edge-preserving filtering in the bilateral grid, tracking the pixel count or weight per grid cell is essential. We store homogeneous coordinates $(\Gamma_{ijk} \mathbf{W}_{ijk}, \mathbf{W}_{ijk})$ during grid creation. Here, \mathbf{W} is derived from Eq. (2) $\mathbf{W} = \mathcal{D}(\mathbf{J}, \mathbf{G}; \mathcal{K})$, with \mathbf{J} as a tensor of ones. This facilitates weighted average calculations and normalizations. Homogeneous coordinate \mathbf{W} indicates the importance of its corresponding data \mathbf{V} . In practice, \mathbf{W} is obtained as an extra output channel, corresponding to \mathbf{J} serving an additional input channel, alongside the image data.

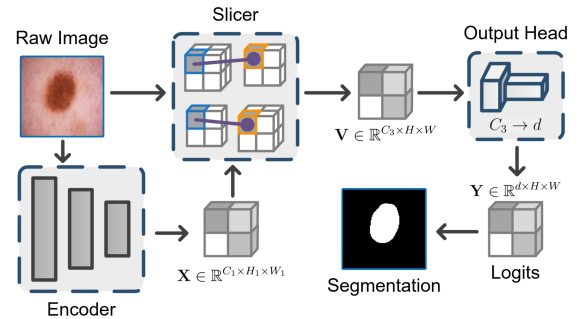


Figure 3: Overview of the Slicer Network framework. The raw image generates a guidance map and an encoder-derived feature map, approximating low-frequency segmentation context. The slicer then refines and upsamples this map, leading to the final segmentation logits via an output head.

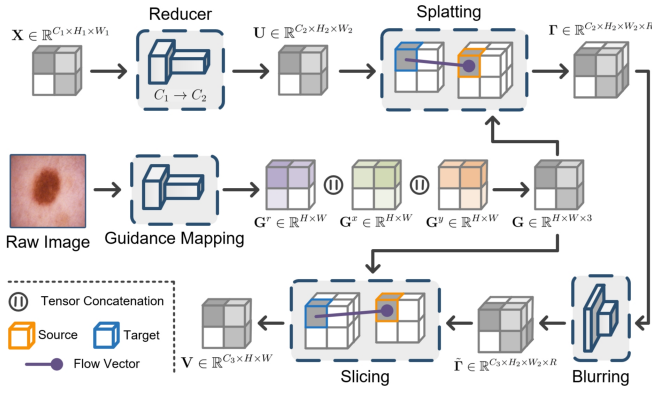


Figure 4: Visual illustration of the Slicer. Details on the splatting and slicing processes are discussed in Section 3.2. The network’s reducer, guidance mapping, and blurring components consist of convolutional layers.

3.3 The Slicer Network

Modern neural networks typically employ an encoder-decoder architecture such as Unet [Ronneberger *et al.*, 2015] for dense mapping tasks. However, their *effective receptive field* (ERF) [Luo *et al.*, 2016] is Gaussian and covers only part of the theoretical receptive field. Consecutive up-sampling layers may maintain the theoretical field but reduce the ERF, as shown in Fig. 1. Upsampling directly from the encoder output preserves the ERF but may result in loss of details. The Slicer Network, featuring an encoder and an edge-preserving slicer (see Fig. 3 for a visual depiction), addresses this issue by allowing direct upsampling from the encoder output, retaining the ERF without losing details.

The Slicer Framework. Central to the Slicer Network, as shown in Fig. 4, is the slicer. The encoder output $\mathbf{X} \in \mathbb{R}^{C_1 \times H_1 \times W_1}$ is reduced to $\mathbf{U} \in \mathbb{R}^{C_2 \times H_2 \times W_2}$, forming a low-frequency approximation for segmentation or deformation. The guidance map \mathbf{G}^r , combined with mesh grids, creates the sampling grid \mathbf{G} . The feature map \mathbf{U} is then mapped onto a bilateral grid $\mathbf{\Gamma} \in \mathbb{R}^{C_2 \times H_2 \times W_2 \times R}$, which undergoes a ‘blurring’ process via learnable convolution layers to produce the refined grid $\hat{\mathbf{\Gamma}} \in \mathbb{R}^{C_3 \times H_2 \times W_2 \times R}$. Slicing this grid results in the feature map $\mathbf{V} \in \mathbb{R}^{C_3 \times H \times W}$, matching the original spatial dimensions.

Guidance Map Generator. The guidance image \mathbf{G}^r represents the range domain in our bilateral grid. Traditional methods use luminance or RGB channels [Paris and Durand, 2006; Chen *et al.*, 2007], but learned guidance maps [Gharbi *et al.*, 2017] are more effective. Our generator has two convolutional layers: a ReLU-activated first layer and a Sigmoid-activated second layer, producing a single-channel tensor, valued within $[0, 1]$, with spatial dimensions matching the input. This guidance map \mathbf{G}^r , concatenated with mesh grids \mathbf{G}^x and \mathbf{G}^y , forms the full sampling grid \mathbf{G} for splatting and slicing.

Blurring. Traditional bilateral grids use fixed kernels [Chen *et al.*, 2007] or energy functions [Barron and Poole, 2016; Chen *et al.*, 2016] for operations like Gaussian denoising [Paris and Durand, 2006] and Laplacian enhancement [Paris

et al., 2015], but this can be limiting. For example, reshaping a tensor $\mathbf{U} \in \mathbb{R}^{C \times H \times W}$ with $C = C_\Gamma \times R$ into a bilateral grid $\mathbf{\Gamma} \in \mathbb{R}^{C_\Gamma \times H \times W \times R}$ can inadequately capture the range domain. Our method projects feature maps onto a sparse, high-dimensional grid as per Eq. (2), and uses learnable convolutional layers for adaptive filtering.

Reducer. The reducer reduces channel size while doubling the spatial dimensions of the feature map. In transformers, it’s a patch expanding module, mirroring Swin transformers’ patch merging [Liu *et al.*, 2021]. For ConvNets, it functions as a transpose convolution.

3.4 Displacement Field Manipulation

We briefly review deformable image registration (DIR), followed by derivation of displacement field manipulation via a bilateral grid. DIR aligns a moving image \mathbf{I}_m with a fixed image \mathbf{I}_f using spatial mapping $\phi(x) = x + \mathbf{u}(x)$, where $\mathbf{u}(x)$ is the displacement at x in domain $\Omega \subset \mathbb{R}^{H \times W \times D}$. This warps \mathbf{I}_m for voxel correspondence with \mathbf{I}_f , using linear interpolation for non-grid positions. Unsupervised learning estimates deformation field ϕ through a network F_θ , optimizing weights θ via a composite loss function \mathcal{L} . This combines dissimilarity between \mathbf{I}_m and \mathbf{I}_f , and deformation field smoothness:

$$\mathcal{L} = \mathcal{L}_{sim}(\mathbf{I}_f, \mathbf{I}_m \circ \phi) + \mathcal{L}_{sim}(\mathbf{G}_f^r, \mathbf{G}_m^r \circ \phi) + \lambda \mathcal{L}_{reg}(\phi), \quad (4)$$

where \mathbf{G}_f^r and \mathbf{G}_m^r are derived from \mathbf{I}_f and \mathbf{I}_m via guidance mapping. For cardiac registration, we use the loss function defined in Eq. (4). In lung registration, this is augmented with an additional Dice loss using segmentation masks and target registration loss based on keypoints.

Displacement Field Manipulation. Using a bilateral grid, we can create a complete displacement field solely from keypoints. Given moving keypoint $\mathbf{p}_m \in \mathbb{R}^{N \times 3}$ and corresponding fixed keypoints $\mathbf{p}_f \in \mathbb{R}^{N \times 3}$, a sparse displacement field is formed by setting $\mathbf{u}[\mathbf{p}_f(i)] = \mathbf{p}_m(i) - \mathbf{p}_f(i)$ for each $i \in \{1, 2, \dots, N\}$, where $\mathbf{p}_*(i)$ denotes the i th point in the set. For all other points $\mathbf{u}(x)$ is a zero vector. Given the guidance map \mathbf{G}^r derived from either a guidance map generator or the raw image, the sparse displacement field \mathbf{u} can be projected onto a bilateral grid as $\mathbf{\Gamma} = \mathcal{D}(\mathbf{u}, \mathbf{G}; \mathcal{K})$. Here, \mathbf{G} includes mesh grids and \mathbf{G}^r , and \mathcal{K} is a linear sampling kernel. The task then is to minimize the equation $\arg \min_{\hat{\mathbf{\Gamma}}} \sum \|\text{grad}(\hat{\mathbf{\Gamma}})\|^2$, subject to the constraint $\hat{\mathbf{\Gamma}}(x) = \mathbf{\Gamma}(x)$, for every x that $\mathbf{\Gamma}(x) \neq \mathbf{0}$. This is used to fill up the zero values in the grid. The optimization outlined in the equation can be efficiently executed through convolution and seamlessly integrated into neural network training.

4 Applications, Experiments & Results

We evaluate the proposed Slicer Network across three medical image analysis applications: unsupervised cardiac registration using cine-MRI, keypoints-based lung registration between inspiration and expiration phases in CT scans, and skin lesion segmentation through dermoscopy. Common implementation aspects are outlined here, with individual application details discussed in their respective sections.

Model	Avg. (%)	RV (%)	LVM (%)	LVBP (%)	HD95 (mm) ↓	SDlogJ ↓
Initial	58.14	64.50	48.33	61.60	11.95	-
ANTs	71.04	68.61	67.53	76.96	13.15	0.056
Demons	72.37	70.85	69.34	76.93	11.46	0.031
Bspline	74.36	72.18	71.68	79.22	11.18	0.030
VoxelMorph	76.35	74.69	73.19	81.15	9.28	0.049
TransMorph	76.89	75.39	73.52	81.75	9.11	0.049
FourierNet	77.04	75.30	73.88	81.96	9.10	0.045
LKU-Net	77.10	75.16	74.20	81.75	9.14	0.048
DeBG	77.36	76.05	74.41	81.61	8.75	0.042
Res-Slicer	79.20	78.14	76.31	83.15	8.33	0.050

Table 1: Quantitative evaluation of different models on the ACDC dataset, highlighting top scores in bold. Metrics include Average Dice (%), RV Dice (%), LVM Dice (%), LVBP Dice (%), HD95 (mm), and SDlogJ, with a ↓ indicating that lower values are better.

General Implementation Details. Experiments are performed in Python 3.7 using PyTorch 1.9.0 [Paszke *et al.*, 2019]. Training takes place on a machine with an A100 GPU, 32GB of memory, and a 16-core CPU. Splatting is based on CUDA code from [Zhang *et al.*, 2023b], compiled with CUDA 11.1. For slicing, PyTorch’s `grid_sample()` function is used. Hyperparameters are optimized using grid search for all methods.

4.1 Cardiac Cine-MRI Registration

The ACDC dataset, with 150 subjects (100 for training, 50 for testing), is used for cardiac registration. Each subject has End-diastole (ED) and End-systole (ES) phase images with segmentation masks. The intra-subject registration requires aligning images from both ED to ES and ES to ED, yielding 300 training pairs ($[100 + 50] \times 2$). We use 170 pairs for training, 30 for validation, and the remaining 100 pairs for testing. All images are resampled to $1.8 \times 1.8 \times 10$ mm spacing and processed to a size of $128 \times 128 \times 16$.

Why Cardiac Registration. Cardiac registration between ED→ES and ES→ED presents a unique challenge due to its asymmetrical nature. Key objects like the left ventricular myocardium (LVM), left ventricle blood pool (LVBP), and right ventricle (RV) show smooth internal contrasts but differ across edges. This aligns with the Slicer Network’s assumption, as the displacement fields required are also *piece-wise smooth*.

Baseline Methods. We benchmark the Slicer Network against leading registration models including VoxelMorph [Balakrishnan *et al.*, 2019], TransMorph [Chen *et al.*, 2022], LKU-Net [Jia *et al.*, 2022], and Fourier-Net [Jia *et al.*, 2023]. Traditional methods ANTs [Avants *et al.*, 2011], Demons [Vercauteren *et al.*, 2007], and Bspline [Marstal *et al.*, 2016] are also included. Additionally, we include an implementation of the deep bilateral grid (denoted as DeBG), previously utilized in image manipulation [Gharbi *et al.*, 2017] and stereo matching [Xu *et al.*, 2021], as another comparative baseline.

Implementation Details. Our network, optimized using the Adam optimizer with a learning rate of $1e-4$, a batch size of 4, and cosine decay, trains for 500 epochs. We employ Mean Square Error (MSE) for similarity loss and an L2 norm on deformation field spatial gradients as a smoothness regularizer ($\lambda = 0.01$), following [Dalca *et al.*, 2019; Balakrishnan *et al.*, 2019], with seven integration steps in the diffeomorphic layer. All deep learning models follow these settings. For our method, named Res-Slicer, we use a ResNet-like encoder. The

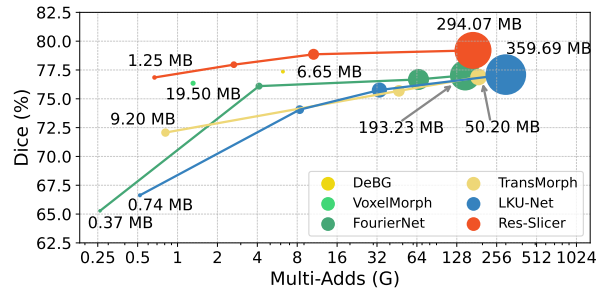


Figure 5: Trade-off between average Dice (%) and computational complexity for the ACDC dataset, comparing parameter size and multi-add operations (in G) on a log-scaled x-axis. TransMorph is shown in three complexities: tiny, small, and normal. Complexity for FourierNet, LKU-Net, and Res-Slicer is adjusted by varying the network’s initial channel count.

guidance map is sourced from the fixed image’s feature map, with MSE loss applied between the fixed and moving images post-guidance convolution. For DeBG, aside from the encoder and splatting adapted from [Ghafoorian *et al.*, 2017; Xu *et al.*, 2021], all other aspects align with our Res-Slicer setup. For DeBG, FourierNet, and Res-Slicer, downsampling is omitted in the axial direction due to thickness considerations.

Evaluation Metrics. Aligned with standard practices [Balakrishnan *et al.*, 2019; Chen *et al.*, 2022], our evaluation uses the Dice Similarity Coefficient (Dice) and the 95th percentile Hausdorff Distance (HD95) for anatomical alignment. We evaluate diffeomorphism quality using the standard deviation of the Jacobian determinant’s logarithm (SDlogJ). Additionally, network complexity is assessed by measuring parameter size and multi-add operations.

Registration Accuracy. Table 1 presents a comparison of methods, showing all produced smooth displacement fields with low SDlogJ. Learning-based methods generally surpass traditional ones in accuracy. Res-Slicer leads in all accuracy metrics, with DeBG, using shuffled channels for range dimension, outperforming others but not matching Res-Slicer. FourierNet competes well, achieving accuracy comparable to other methods but with reduced complexity. This suggests that increasing the *effective receptive field (ERF)* through strategic upsampling from deeper feature maps is beneficial for cardiac registration. Results from Res-Slicer and DeBG emphasize the importance of maintaining edge detail.

Complexity Analysis. We evaluate network complexity using parameter size (MB) and multi-add operations (G). Complexity is adjusted based on the parameter size for each network. Fig. 5 compares the accuracy and complexity of Res-Slicer against other methods. Res-Slicer shows an optimal trade-off; with comparable Dice (76.85%), it reduces parameter size and multi-add operations by 81.0% and 89.0% relative to DeBG, and by 99.7% and 99.8% compared to LKU-Net.

4.2 Keypoints-Based Lung CT Registration

We use a lung CT dataset [Hering *et al.*, 2020] for keypoints-based image registration, featuring 20 subjects with paired expiration and inspiration phase scans. Each scan includes

Model	Lung (%)	TRE (mm) ↓	HD95 (mm) ↓	SDlogJ ↓
Initial	79.53	14.64	206.45	-
TransMorph	93.25	10.23	160.07	0.143
VoxelMorph	93.44	10.37	53.61	0.197
FourierNet	93.98	8.74	18.36	0.205
LKU-Net	94.91	8.44	12.30	0.218
Zero-Shot (KPS)	83.36	2.35	186.52	0.304
Point-Slicer	95.77	2.66	16.431	0.221
Zero-Shot (LMS)	80.21	0.20	207.50	0.220

Table 2: Quantitative evaluation of different models on the Lung CT dataset, highlighting top scores in bold. Metrics include Average Dice of lung region (%), TRE (mm), HD95 (mm), and SDlogJ, with a ↓ indicating that lower values are better.

auto-generated keypoints with corresponding matches in both phases. For testing, manual landmarks are available for three subjects, with the remaining 17 used for training. CT scans, sized $192 \times 192 \times 208$, are preprocessed to a voxel spacing of $1.75 \times 1.25 \times 1.75$ mm.

Why Lung CT Registration. Lung CT registration between expiration and inspiration phases present large and complex lung deformations. This process requires accurate alignment of both expansive anatomical regions and specific landmarks. Existing models often struggle with the sparse keypoints in unsupervised registration. The Slicer Network uniquely addresses this by offering zero-shot learning from keypoints (as elaborated in Sec. 3.4) for generating deformation fields, seamlessly incorporating these elements into its training process.

Baseline Methods & Evaluation Metrics. For lung CT registration, we maintain the same learning-based baseline methods used in cardiac registration, excluding DeBG due to its inability to handle keypoints with channel-based range representation. Alongside the metrics previously employed, we introduce the Target Registration Error of landmarks (TRE) to our evaluation criteria.

Implementation Details. Training parallels cardiac registration, with modifications including a batch size of 1 and 200 total epochs. We incorporate Dice and TRE losses ($\lambda = 0.1$). Our method, named Point-Slicer, uses LKU-Net as the backbone. The fixed image undergoes guidance mapping, followed by keypoints being projected onto a bilateral grid. This gener-

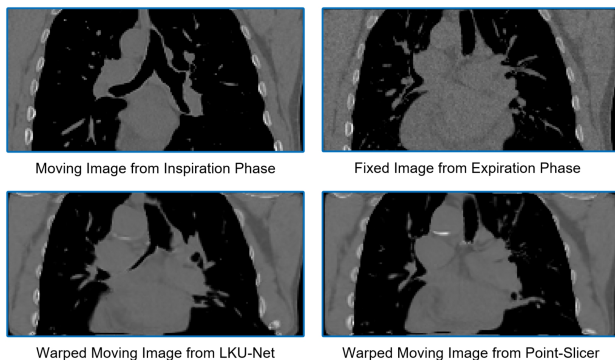


Figure 6: Visual comparison of lung CT dataset registration quality between LKU-Net and our Point-Slicer. The inspiration scan and its warped counterpart are cropped to match the expiration scan’s size due to the lungs’ partial visibility.

Model	Dice (%)	Prec (%)	Sens (%)	F1 Score (%)	HD95 ↓
Unet	84.34	87.41	87.39	87.40	23.66
Att-Unet	85.84	85.77	90.75	88.19	21.50
SAM	87.20	84.57	93.48	88.80	17.74
Polyp-PVT	88.14	86.95	93.09	89.92	17.05
Swin-Unet	88.35	89.10	91.00	90.04	17.95
PVT-Cascade	88.51	87.23	92.65	89.86	16.55
Tran-Unet	88.93	86.76	94.40	90.42	16.60
Swin-Slicer	90.02	90.57	92.12	91.34	15.16

Table 3: Quantitative evaluation of different models on the test set of ISIC2018 dataset, highlighting top scores in bold. Metrics include Average Dice (%), Prec (%), Sens (%), F1 Score (%) and HD95 (in pixels), with a down arrow indicating that lower values are better.

ates a dense displacement field (described in Sec. 3.4), which is then used to warp the moving image prior to its processing through the backbone. Zero-Shot (KPS) involves using the displacement field generated from raw fixed images and auto-generated keypoints (KPS) as the final outcome. Zero-Shot (LMS) uses ground-truth landmarks (LMS) as a reference and for analytical purposes only. Both Zero-Shot learners apply the method outlined in Sec. 3.4, relying on raw fixed images instead of learnable guidance mapping.

Registration Accuracy. Table 2 compares various methods, including Zero-Shot learners. Zero-Shot (KPS) excels in TRE but lags in Dice and HD95, due to its well-aligned lung landmarks but sparse keypoints leading to inadequate lung boundary alignment. Point-Slicer, utilizing both keypoints and lung mask data, attains a well-balanced Dice and TRE, leading to improved anatomical region alignment, as depicted in Fig. 6, outperforming other techniques. Zero-Shot (LMS), using landmark-generated fields, shows low TRE, indicating that improved keypoint descriptors could enhance landmark alignment performance. This also points to Point-Slicer’s potential for end-to-end joint training of keypoint descriptor and anatomical region alignment, a direction for future research.

4.3 Skin Lesion Segmentation

We evaluate the Slicer Network for skin lesion segmentation using the ISIC2018 dataset [Codella *et al.*, 2019; Tschandl *et al.*, 2018], comprising 2594 training, 100 validation, and 1000 testing images. Adhering to the official dataset divisions for training, validation, and testing, as specified on the dataset’s website¹, we ensure consistency and repeatability without manual data partitioning.

Why Skin Lesion Segmentation. Dermoscopic skin lesion segmentation presents a unique challenge due to the variability in lesion shapes, sizes, and textures, despite consistent internal textures. This scenario aligns well with the Slicer Network’s design assumption, particularly as the resulting segmentation masks are *piece-wise constant*.

Baseline Methods. We evaluate the Slicer Network against leading models including SAM [Kirillov *et al.*, 2023], TransUnet [Chen *et al.*, 2021], Swin-Unet [Cao *et al.*, 2022], Polyp-PVT [Dong *et al.*, 2023], PVT-Cascade [Rahman and Marculescu, 2023], Unet [Ronneberger *et al.*, 2015], and Att-Unet [Oktay *et al.*, 2018], fine-tuning the SAM backbone without

¹<https://challenge.isic-archive.com/landing/2018>

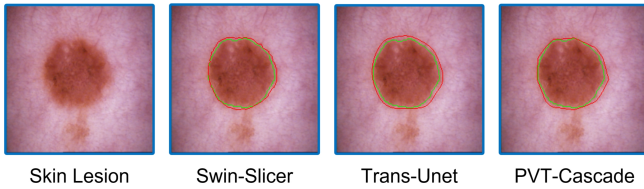


Figure 7: Qualitative segmentation results from the top-performing methods based on Dice scores: Swin-Slicer, Trans-Unet, and PVT-Cascade. The green contour represents the ground truth delineation of the lesion, and the red contour indicates the model’s prediction.

additional prompts.

Implementation Details and Evaluation Metrics. Training employs the Adam optimizer [Kingma and Ba, 2014] with an initial learning rate of $1e-4$ and a multi-step scheduler reducing it by half at 50%, 70%, and 90% of the 70 total epochs. Images are resized to $(224, 224)$, with batches of 16. Segmentation is evaluated using Dice for overlap, Sensitivity (Sens), Precision (Prec), and F1-score (the harmonic mean) for detection accuracy, along with HD95 (in pixels) for boundary precision. Our network, termed Swin-Slicer, incorporates the Swin transformer’s tiny version [Liu *et al.*, 2021] as encoder.

Segmentation Accuracy. Table 3 shows Swin-Slicer outperforming transformer-based and traditional ConvNet methods on the ISIC2018 dataset in Dice, F1-Score, and HD95. This demonstrates superior segmentation precision and boundary adherence. While Trans-Unet shows highest sensitivity, it lags in precision. In contrast, Swin-Slicer achieves a balanced trade-off, leading in F1-Score without sacrificing sensitivity.

Qualitative Results. Swin-Slicer effectively uses just a 7×7 feature map from the Swin transformer encoder for the slicer, yet, as Fig. 7 shows, it achieves superior delineation of lesion boundary. This success is attributed to maintaining the ERF by slicing directly from the lifted bilateral grid, coupled with the guidance map from raw images preserving lesion boundary details.

4.4 Discussions

Effects of Sampling Rate s_r . The sampling rate s_r affects the range domain (\mathcal{R}). At $s_r = 1$, the range dimension simplifies to 1, transforming the process into a gated attention where the attention map, derived from the guidance map, gates the linearly upsampled encoder output. Decreasing s_r increase the dimensionality in range domain and enhances edge distinction in spatial domain but also increases computational demands. Experimentally, reducing s_r from $s_r = 1$ to $s_r = 1/64$ reveals that accuracy in cardiac, lung registration, and lesion segmentation improves as s_r decreases, reaching optimal points at $s_r = 1/8$, $s_r = 1/8$, and $s_r = 1/32$, respectively, before declining. The smaller optimal s_r for lesion segmentation reflects its greater need for precise boundary handling.

Effects of Sampling Rate s_s . The sampling rate s_s influences the spatial domain (\mathcal{S}). At $s_s = 1$, spatial dimensions match the original image. Increasing s_s results in smoother outcomes, larger ERF in neural networks, and reduced computational load. Increasing s_s from $s_s = 1$ to $s_s = 32$ improves

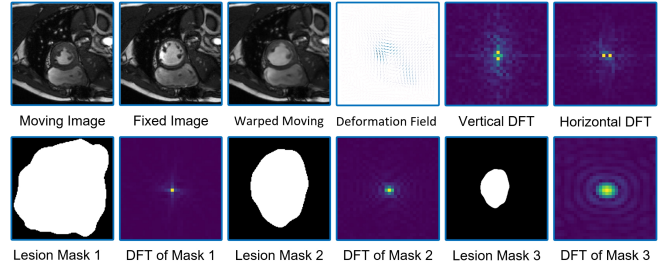


Figure 8: The first row shows cardiac registration visualizations with Res-Slicer, displaying 32×32 resized 2D deformation fields and their Discrete Fourier Transforms (DFTs) for clarity. The second row features lesion masks and their DFTs, with lesion mask 3 being a smaller scaled version of mask 2. DFT magnitudes are normalized to $(0,1)$ and resized to 32×32 for enhanced visualization quality.

accuracy in cardiac and lung registration, and lesion segmentation, peaking at $s_s = 8$ for registrations and $s_s = 32$ for segmentation, then decreasing. The higher optimal $s_s = 32$ for lesion segmentation is consistent with the spectrum analysis below.

Spectrum Analysis. Fig. 8 shows the outcome deformation field from cardiac registration and binary masks from skin lesion segmentation, along with their magnitude spectrums. Larger masks tend to concentrate more in the low-frequency range. Additionally, the deformation field exhibits more higher-frequency components compared to the lesion mask, reflecting the varying spatial sampling rates needed for image registration versus lesion segmentation. While spectrum analysis has previously been applied in image registration [Jia *et al.*, 2023; Wang and Zhang, 2020] and segmentation [Zhou *et al.*, 2023] and proved effective for certain applications, our work is unique in introducing a unified framework aimed at enhancing a broad range of medical applications.

Limitations. The development of the Slicer Network has revealed three key limitations. First, its suitability is limited for applications demanding high-frequency components in the output, such as curvilinear structure segmentation and small targets detection. Second, while the bilateral grid is effective, more efficient high-dimensional filtering methods like adaptive manifolds [Gastal and Oliveira, 2012] could offer improvements. Finally, the guidance map generation, essentially a metric learning process, remains an area for further exploration and development.

5 Conclusions

Our paper introduces the Slicer Network, a novel neural network architecture for medical image analysis, effectively addressing two questions from Sec. 1. For **Q1**, the network incorporates a learnable cross-bilateral grid with guidance mapping, enhancing the *effective receptive field* while preserving boundary details. For **Q2**, in scenarios where both input images and outcomes are *piece-wise smooth*, the Slicer Network offers reduced computational demands without sacrificing accuracy. Its proven effectiveness across three medical applications indicates potential advantages for other medical tasks that meet the same underlying assumption.

References

- [Adams *et al.*, 2009] Andrew Adams, Natasha Gelfand, Jennifer Dolson, and Marc Levoy. Gaussian kd-trees for fast high-dimensional filtering. In *ACM SIGGRAPH 2009 Papers*, SIGGRAPH '09, New York, NY, USA, 2009. Association for Computing Machinery.
- [Avants *et al.*, 2011] Brian B Avants, Nicholas J Tustison, Gang Song, Philip A Cook, Arno Klein, and James C Gee. A Reproducible Evaluation of ANTs Similarity Metric Performance in Brain Image Registration. *Neuroimage*, 54(3):2033–2044, 2011.
- [Balakrishnan *et al.*, 2019] Guha Balakrishnan, Amy Zhao, Mert R Sabuncu, John Guttag, and Adrian V Dalca. Voxelmorph: a learning framework for deformable medical image registration. *IEEE transactions on medical imaging*, 38(8):1788–1800, 2019.
- [Ballard, 1981] Dana H Ballard. Generalizing the hough transform to detect arbitrary shapes. *Pattern recognition*, 13(2):111–122, 1981.
- [Barron and Poole, 2016] Jonathan T Barron and Ben Poole. The fast bilateral solver. In *European conference on computer vision*, pages 617–632. Springer, 2016.
- [Cao *et al.*, 2022] Hu Cao, Yueyue Wang, Joy Chen, Dongsheng Jiang, Xiaopeng Zhang, Qi Tian, and Manning Wang. Swin-unet: Unet-like pure transformer for medical image segmentation. In *European conference on computer vision*, pages 205–218. Springer, 2022.
- [Chen *et al.*, 2007] Jiawen Chen, Sylvain Paris, and Frédo Durand. Real-time edge-aware image processing with the bilateral grid. *ACM Transactions on Graphics (TOG)*, 26(3):103–es, 2007.
- [Chen *et al.*, 2016] Jiawen Chen, Andrew Adams, Neal Wadhwa, and Samuel W Hasinoff. Bilateral guided upsampling. *ACM Transactions on Graphics (TOG)*, 35(6):1–8, 2016.
- [Chen *et al.*, 2021] Jieneng Chen, Yongyi Lu, Qihang Yu, Xiangde Luo, Ehsan Adeli, Yan Wang, Le Lu, Alan L Yuille, and Yuyin Zhou. Transunet: Transformers make strong encoders for medical image segmentation. *arXiv preprint arXiv:2102.04306*, 2021.
- [Chen *et al.*, 2022] Junyu Chen, Eric C Frey, Yufan He, William P Segars, Ye Li, and Yong Du. Transmorph: Transformer for unsupervised medical image registration. *Medical image analysis*, 82:102615, 2022.
- [Codella *et al.*, 2019] Noel Codella, Veronica Rotemberg, Philipp Tschandl, M Emre Celebi, Stephen Dusza, David Gutman, Brian Helba, Aadi Kalloo, Konstantinos Liopyris, Michael Marchetti, et al. Skin lesion analysis toward melanoma detection 2018: A challenge hosted by the international skin imaging collaboration (isic). *arXiv preprint arXiv:1902.03368*, 2019.
- [Dalca *et al.*, 2019] Adrian V Dalca, Guha Balakrishnan, John Guttag, and Mert R Sabuncu. Unsupervised Learning of Probabilistic Diffeomorphic Registration for Images and Surfaces. *Medical Image Analysis*, 57:226–236, 2019.
- [Ding *et al.*, 2022] Xiaohan Ding, Xiangyu Zhang, Jungong Han, and Guiguang Ding. Scaling up your kernels to 31x31: Revisiting large kernel design in cnns. In *Proceedings of the IEEE/CVF conference on computer vision and pattern recognition*, pages 11963–11975, 2022.
- [Dong *et al.*, 2023] Bo Dong, Wenhai Wang, Deng-Ping Fan, Jinpeng Li, Huazhu Fu, and Ling Shao. Polyp-pvt: Polyp segmentation with pyramid vision transformers. *CAAI AIR*, 2023.
- [Dosovitskiy *et al.*, 2021] Alexey Dosovitskiy, Lucas Beyer, Alexander Kolesnikov, Dirk Weissenborn, Xiaohua Zhai, Thomas Unterthiner, Mostafa Dehghani, Matthias Minderer, Georg Heigold, Sylvain Gelly, et al. An image is worth 16x16 words: Transformers for image recognition at scale. In *International Conference on Learning Representations*, 2021.
- [Gastal and Oliveira, 2012] Eduardo SL Gastal and Manuel M Oliveira. Adaptive manifolds for real-time high-dimensional filtering. *ACM Transactions on Graphics (TOG)*, 31(4):1–13, 2012.
- [Genzel *et al.*, 2022] Martin Genzel, Ingo Gühring, Jan Macdonald, and Maximilian März. Near-exact recovery for tomographic inverse problems via deep learning. In *International Conference on Machine Learning*, pages 7368–7381. PMLR, 2022.
- [Ghafoorian *et al.*, 2017] Mohsen Ghafoorian, Nico Karssemeijer, Tom Heskes, Mayra Bergkamp, Joost Wissink, Jiri Obels, Karlijn Keizer, Frank-Erik de Leeuw, Bram Van Ginneken, Elena Marchiori, et al. Deep multi-scale location-aware 3d convolutional neural networks for automated detection of lacunes of presumed vascular origin. *NeuroImage: Clinical*, 14:391–399, 2017.
- [Gharbi *et al.*, 2017] Michaël Gharbi, Jiawen Chen, Jonathan T Barron, Samuel W Hasinoff, and Frédo Durand. Deep bilateral learning for real-time image enhancement. *ACM Transactions on Graphics (TOG)*, 36(4):1–12, 2017.
- [He *et al.*, 2016] Kaiming He, Xiangyu Zhang, Shaoqing Ren, and Jian Sun. Deep residual learning for image recognition. In *Proceedings of the IEEE conference on computer vision and pattern recognition*, pages 770–778, 2016.
- [Helgason and Helgason, 1999] Sigurdur Helgason and S Helgason. *The radon transform*, volume 2. Springer, 1999.
- [Hering *et al.*, 2020] A Hering, K Murphy, and B van Ginneken. Learn2reg challenge: Ct lung registration-training data, may 2020. DOI: <https://doi.org/10.5281/zenodo.3835682>, 2020.
- [Isensee *et al.*, 2021] Fabian Isensee, Paul F Jaeger, Simon AA Kohl, Jens Petersen, and Klaus H Maier-Hein. nnu-net: a self-configuring method for deep learning-based biomedical image segmentation. *Nature methods*, 18(2):203–211, 2021.
- [Jaderberg *et al.*, 2015] Max Jaderberg, Karen Simonyan, Andrew Zisserman, et al. Spatial transformer networks. *Advances in neural information processing systems*, 28, 2015.
- [Jampani *et al.*, 2016] Varun Jampani, Martin Kiefel, and Peter V Gehler. Learning sparse high dimensional filters: Image filtering, dense crfs and bilateral neural networks. In *Proceedings of the IEEE Conference on Computer Vision and Pattern Recognition*, pages 4452–4461, 2016.
- [Jia *et al.*, 2022] Xi Jia, Joseph Bartlett, Tianyang Zhang, Wenqi Lu, Zhaowen Qiu, and Jinming Duan. U-net vs transformer: Is u-net outdated in medical image registration? In *International Workshop on Machine Learning in Medical Imaging*, pages 151–160. Springer, 2022.
- [Jia *et al.*, 2023] Xi Jia, Joseph Bartlett, Wei Chen, Siyang Song, Tianyang Zhang, Xinxing Cheng, Wenqi Lu, Zhaowen Qiu, and Jinming Duan. Fourier-net: Fast image registration with band-limited deformation. *Proceedings of the AAAI Conference on Artificial Intelligence*, 37(1):1015–1023, Jun. 2023.
- [Kingma and Ba, 2014] Diederik P Kingma and Jimmy Ba. Adam: A method for stochastic optimization. *arXiv preprint arXiv:1412.6980*, 2014.
- [Kirillov *et al.*, 2023] Alexander Kirillov, Eric Mintun, Nikhila Ravi, Hanzi Mao, Chloe Rolland, Laura Gustafson, Tete Xiao, Spencer Whitehead, Alexander C. Berg, Wan-Yen Lo, Piotr Dollar, and Ross Girshick. Segment anything. In *Proceedings of the*

- IEEE/CVF International Conference on Computer Vision (ICCV)*, pages 4015–4026, October 2023.
- [Kopf *et al.*, 2007] Johannes Kopf, Michael F Cohen, Dani Lischinski, and Matt Uyttendaele. Joint bilateral upsampling. *ACM Transactions on Graphics (ToG)*, 26(3):96–es, 2007.
- [Lee *et al.*, 2022] Ho Hin Lee, Shunxing Bao, Yuankai Huo, and Bennett A Landman. 3d ux-net: A large kernel volumetric convnet modernizing hierarchical transformer for medical image segmentation. *arXiv preprint arXiv:2209.15076*, 2022.
- [Lin *et al.*, 2020] Yancong Lin, Silvia L Pinteá, and Jan C van Gemert. Deep hough-transform line priors. In *European Conference on Computer Vision*, pages 323–340. Springer, 2020.
- [Liu *et al.*, 2021] Ze Liu, Yutong Lin, Yue Cao, Han Hu, Yixuan Wei, Zheng Zhang, Stephen Lin, and Baining Guo. Swin transformer: Hierarchical vision transformer using shifted windows. In *Proceedings of the IEEE/CVF International Conference on Computer Vision*, pages 10012–10022, 2021.
- [Liu *et al.*, 2022] Zhuang Liu, Hanzi Mao, Chao-Yuan Wu, Christoph Feichtenhofer, Trevor Darrell, and Saining Xie. A convnet for the 2020s. In *Proceedings of the IEEE/CVF conference on computer vision and pattern recognition*, pages 11976–11986, 2022.
- [Luo *et al.*, 2016] Wenjie Luo, Yujia Li, Raquel Urtasun, and Richard Zemel. Understanding the effective receptive field in deep convolutional neural networks. *Advances in neural information processing systems*, 29, 2016.
- [Marstal *et al.*, 2016] Kasper Marstal, Floris Berendsen, Marius Staring, and Stefan Klein. SimpleElastix: A User-friendly, Multilingual Library for Medical Image Registration. In *Proceedings of the IEEE Conference on Computer Vision and Pattern Recognition Workshops*, pages 134–142, 2016.
- [Oktay *et al.*, 2018] Ozan Oktay, Jo Schlemper, Loic Le Folgoc, Matthew Lee, Mattias Heinrich, Kazunari Misawa, Kensaku Mori, Steven McDonagh, Nils Y Hammerla, Bernhard Kainz, et al. Attention u-net: Learning where to look for the pancreas. *arXiv preprint arXiv:1804.03999*, 2018.
- [Paris and Durand, 2006] Sylvain Paris and Frédo Durand. A fast approximation of the bilateral filter using a signal processing approach. In *Computer Vision—ECCV 2006: 9th European Conference on Computer Vision, Graz, Austria, May 7–13, 2006, Proceedings, Part IV 9*, pages 568–580. Springer, 2006.
- [Paris *et al.*, 2015] Sylvain Paris, Samuel W Hasinoff, and Jan Kautz. Local laplacian filters: edge-aware image processing with a laplacian pyramid. *Communications of the ACM*, 58(3):81–91, 2015.
- [Paszke *et al.*, 2019] Adam Paszke, Sam Gross, Francisco Massa, Adam Lerer, James Bradbury, Gregory Chanan, Trevor Killeen, Zeming Lin, Natalia Gimelshein, Luca Antiga, et al. Pytorch: An imperative style, high-performance deep learning library. *Advances in neural information processing systems*, 32, 2019.
- [Rahman and Marculescu, 2023] Md Mostafijur Rahman and Radu Marculescu. Medical image segmentation via cascaded attention decoding. In *Proceedings of the IEEE/CVF Winter Conference on Applications of Computer Vision*, pages 6222–6231, 2023.
- [Ridnik *et al.*, 2021] Tal Ridnik, Emanuel Ben-Baruch, Asaf Noy, and Lihi Zelnik-Manor. Imagenet-21k pretraining for the masses. *arXiv preprint arXiv:2104.10972*, 2021.
- [Ronneberger *et al.*, 2015] Olaf Ronneberger, Philipp Fischer, and Thomas Brox. U-net: Convolutional networks for biomedical image segmentation. In *Medical Image Computing and Computer-Assisted Intervention—MICCAI 2015: 18th International Conference, Munich, Germany, October 5–9, 2015, Proceedings, Part III 18*, pages 234–241. Springer, 2015.
- [Smith and Brady, 1997] Stephen M Smith and J Michael Brady. Susan—a new approach to low level image processing. *International journal of computer vision*, 23(1):45–78, 1997.
- [Sun *et al.*, 2017] Chen Sun, Abhinav Shrivastava, Saurabh Singh, and Abhinav Gupta. Revisiting unreasonable effectiveness of data in deep learning era. In *Proceedings of the IEEE international conference on computer vision*, pages 843–852, 2017.
- [Tang *et al.*, 2022] Yucheng Tang, Dong Yang, Wenqi Li, Holger R Roth, Bennett Landman, Daguang Xu, Vishwesh Nath, and Ali Hatamizadeh. Self-supervised pre-training of swin transformers for 3d medical image analysis. In *Proceedings of the IEEE/CVF Conference on Computer Vision and Pattern Recognition*, pages 20730–20740, 2022.
- [Tomasi and Manduchi, 1998] Carlo Tomasi and Roberto Manduchi. Bilateral filtering for gray and color images. In *Sixth international conference on computer vision (IEEE Cat. No. 98CH36271)*, pages 839–846. IEEE, 1998.
- [Tschandl *et al.*, 2018] Philipp Tschandl, Cliff Rosendahl, and Harald Kittler. The ham10000 dataset, a large collection of multi-source dermatoscopic images of common pigmented skin lesions. *Scientific data*, 5(1):1–9, 2018.
- [Vaswani *et al.*, 2017] Ashish Vaswani, Noam Shazeer, Niki Parmar, Jakob Uszkoreit, Llion Jones, Aidan N Gomez, Łukasz Kaiser, and Illia Polosukhin. Attention is all you need. *Advances in neural information processing systems*, 30, 2017.
- [Vercauteren *et al.*, 2007] Tom Vercauteren, Xavier Pennec, Aymeric Perchant, Nicholas Ayache, et al. Diffeomorphic Demons Using ITK’s Finite Difference Solver Hierarchy. *The Insight Journal*, 1, 2007.
- [Wang and Zhang, 2020] Jian Wang and Miaomiao Zhang. Deep-flash: An efficient network for learning-based medical image registration. In *Proceedings of the IEEE/CVF conference on computer vision and pattern recognition*, pages 4444–4452, 2020.
- [Wang *et al.*, 2021] Wenhai Wang, Enze Xie, Xiang Li, Deng-Ping Fan, Kaitao Song, Ding Liang, Tong Lu, Ping Luo, and Ling Shao. Pyramid vision transformer: A versatile backbone for dense prediction without convolutions. In *Proceedings of the IEEE/CVF international conference on computer vision*, pages 568–578, 2021.
- [Xu *et al.*, 2021] Bin Xu, Yuhua Xu, Xiaoli Yang, Wei Jia, and Yulan Guo. Bilateral grid learning for stereo matching networks. In *Proceedings of the IEEE/CVF Conference on Computer Vision and Pattern Recognition*, pages 12497–12506, 2021.
- [Zhang *et al.*, 2023a] Hang Zhang, Xiang Chen, Rongguang Wang, Renjiu Hu, Dongdong Liu, and Gaolei Li. Spatially covariant image registration with text prompts. *arXiv preprint arXiv:2311.15607*, 2023.
- [Zhang *et al.*, 2023b] Hang Zhang, Rongguang Wang, Renjiu Hu, Jinwei Zhang, and Jiahao Li. Deda: Deep directed accumulator. In *Medical Image Computing and Computer Assisted Intervention – MICCAI 2023*, pages 765–775, Cham, 2023. Springer Nature Switzerland.
- [Zhang *et al.*, 2023c] Hang Zhang, Rongguang Wang, Jinwei Zhang, Dongdong Liu, Chao Li, and Jiahao Li. Spatially covariant lesion segmentation. In Edith Elkind, editor, *Proceedings of the Thirty-Second International Joint Conference on Artificial Intelligence*,

IJCAI-23, pages 1713–1721. International Joint Conferences on Artificial Intelligence Organization, 8 2023. Main Track.

[Zhao *et al.*, 2021] Kai Zhao, Qi Han, Chang-Bin Zhang, Jun Xu, and Ming-Ming Cheng. Deep hough transform for semantic line detection. *IEEE Transactions on Pattern Analysis and Machine Intelligence*, 2021.

[Zhou *et al.*, 2023] Yanfeng Zhou, Jiaying Huang, Chenlong Wang, Le Song, and Ge Yang. Xnet: Wavelet-based low and high frequency fusion networks for fully-and semi-supervised semantic segmentation of biomedical images. In *Proceedings of the IEEE/CVF International Conference on Computer Vision*, pages 21085–21096, 2023.